geomatics

MDPI

Article

Assessing the Accuracy of GNSS Velocities: A Multi-Software Comparison of Differential and PPP-AR Solutions

Shahriar Mokhtari [1,*], Antonio Zanutta [1], Monia Negusini [2], Matteo Cappuccio [1], Giorgio Del Ciondolo [1], Domitilla Forina [3], Alessandro Capra [4] and Luca Vittuari [1]

[1] Department of Civil, Chemical, Environmental, and Materials Engineering (DICAM), Alma Mater Studiorum University of Bologna, 40136 Bologna, Italy; antonio.zanutta@unibo.it (A.Z.); matteo.cappuccio@unibo.it (M.C.); giorgio.delciondolo2@unibo.it (G.D.C.); luca.vittuari@unibo.it (L.V.)
[2] Institute of Radioastronomy (IRA), National Institute for Astrophysics (INAF), 40129 Bologna, Italy; monia.negusini@inaf.it
[3] Department of Environmental Sciences, Informatics and Statistics, Ca' Foscari University of Venice, Mestre, 30172 Venice, Italy; domitilla.forina@unimore.it
[4] Department of Engineering "Enzo Ferrari" (DIEF), University of Modena and Reggio Emilia, 41125 Modena, Italy; alessandro.capra@unimore.it
* Correspondence: shahriar.mokhtari5@unibo.it

Abstract

Precise Point Positioning with Ambiguity Resolution (PPP-AR) has emerged as a viable alternative to traditional network-based GNSS processing for crustal deformation monitoring and velocity field estimation. It provides high-precision daily coordinate solutions with simpler logistics, particularly for densifying velocity fields in regions lacking dense GNSS infrastructure. This study evaluates whether long-term velocity estimates derived from independent operational GNSS processing chains remain mutually consistent for regional geodynamic applications. We applied four processing strategies to 79 high-quality continuous GNSS stations in Southern Italy over the period 2017–2024: a Bernese double-difference network solution used as reference, Bernese PPP-AR, PRIDE PPP-AR, and the Nevada Geodetic Laboratory (NGL) PPP-AR solution derived from the GipsyX processing pipeline. The daily coordinate series preserve the realistic differences among the processing chains, while the subsequent velocity estimation was performed with a common HectorP workflow. A Bland–Altman screening identified 10 outlier stations, and the final inter-comparison is based on the remaining 69 stations (87.3% of the network). The results show that horizontal velocity components derived from PPP-AR agree with the network solution at sub-millimeter-per-year levels, with correlation coefficients exceeding 0.95, indicating strong coherence between the PPP-AR and network-derived horizontal velocity fields. In addition, vertical velocity estimates exhibit processing-strategy-dependent differences on the order of 1 mm yr^{-1} among PPP-AR solutions and relative to the network, indicating that careful interpretation is required for vertical rates. This study presents a systematic comparison of operational PPP-AR velocity solutions and a double-difference reference solution, demonstrating that complete processing-chain differences can introduce vertical effects comparable to those between PPP-AR and network processing. The findings support the practical maturity of PPP-AR for horizontal velocity field densification, while showing that vertical rates remain sensitive to processing strategy at the ∼1 mm yr^{-1} level.

Keywords: Precise Point Positioning (PPP-AR); double-difference processing; GNSS velocity estimation; multi-software comparison; crustal deformation

Check for updates

Academic Editors: João Catalão Fernandes and Gino Dardanelli

Received: 21 April 2026
Revised: 27 May 2026
Accepted: 2 June 2026
Published: 4 June 2026

Copyright: © 2026 by the authors. Licensee MDPI, Basel, Switzerland. This article is an open access article distributed under the terms and conditions of the Creative Commons Attribution (CC BY) license.

1. Introduction

Accurate GNSS-derived velocity fields are fundamental for quantifying tectonic plate motions, crustal deformation, and geodynamic processes, as well as for maintaining precise terrestrial reference frames [1,2]. In recent decades, the geodetic community has dramatically expanded continuous GNSS networks, providing dense spatial coverage and long time series that enable crustal velocities to be determined with ever-increasing precision. For example, European initiatives now combine thousands of GNSS stations into unified multi-year solutions aligned to global reference frames, achieving horizontal velocity consistency at the 0.1–0.2 mm/yr level [1]. These velocity fields serve both scientific and practical needs—from probing intraplate strain accumulation to providing stable ground references for sea-level change—and thus demand the highest possible accuracy and consistency [3]. However, realizing sub-millimeter-per-year velocity precision is challenging, as results can be influenced by the chosen GNSS processing strategy, the handling of temporally correlated noise, and the definition of the reference frame [4,5].

Traditionally, high-precision GNSS analysis has relied on network-based differential processing (using double-differenced observations) to estimate station positions and velocities. This approach, implemented in software such as Bernese GNSS Software v5.4 [6], GAMIT/GLOBK Release 10.35 [7], or GIPSY-OASIS II [8], benefits from relative positioning and usually robust inter-station ambiguity resolution. In parallel, the Precise Point Positioning (PPP) technique emerged as a single-station strategy that determines absolute positions using precise satellite orbits and clocks [8,9]. PPP offers logistical advantages (no need for a local fiducial network) but historically produced float ambiguities, leading to slightly lower horizontal precision and slower convergence compared with network solutions [5,10]. Over the past decade, these approaches have converged through advances in PPP with Ambiguity Resolution (PPP-AR). By applying satellite phase-bias calibrations and fixing integer ambiguities on a single receiver, PPP-AR effectively bridges the performance gap with network methods. Modern PPP-AR implementations (e.g., PRIDE, GipsyX) achieve daily positioning scatter at the few-millimeter level, with vertical accuracy improvements that, while modest, bring the up-component closer to horizontal precision [10,11]. Inter-comparisons confirm that undifferenced ambiguity fixing yields station coordinates and velocities nearly equivalent to classical network solutions. For instance, a four-year experiment by Chen et al. (2024) found that processing a global 139-station network with undifferenced PPP-AR produced velocities within ∼0.1–0.3 mm/yr of a double-differenced solution (differences up to 0.5 mm/yr in the vertical) [12]. Likewise, a regional dual-processing study in the Iberian Peninsula attained sub-millimeter-per-year agreement between velocities derived from GAMIT (network DD) and GipsyX (PPP-AR), with RMS differences on the order of 0.2 mm/yr horizontally and 0.3 mm/yr vertically [13]. These results underscore a growing consensus that modern GNSS software—whether network-based or PPP-AR—can produce consistent velocity estimates at the millimeter-per-year level [14]. Furthermore, the PPP-AR concept has been extended to real-time PPP–RTK services, which achieve centimeter-level positioning accuracy within seconds [15], highlighting the maturity and precision of ambiguity-resolved PPP techniques.

Despite the convergence in capability, subtle discrepancies can still arise among processing strategies, particularly in the vertical component. Differences in data modeling—such as tropospheric delay estimation, non-tidal loading corrections, or reference frame alignment—may lead to small velocity biases if not handled consistently. For instance, Wang et al. (2025) demonstrated that PPP-AR solutions exhibit systematic biases particularly in the vertical component, with RMS differences 3× larger than horizontal (5.10 mm vs. 1.58–2.37 mm) and velocity discrepancies reaching 0.67 mm/yr vertically [14]. In a 16-year dense network solution for Greece, Bitharis et al. (2024) found that vertical

velocities were more scattered, with mean uncertainties of 0.6 mm/yr (roughly three times larger than horizontal) due to seasonal effects, and noted that residual offsets of 1–3 mm/yr between their velocity field and others could be attributed to differing reference frame realizations rather than processing method [2]. Similarly, Chen et al. (2024) observed that undifferenced vs. differenced processing produced slight biases in Helmert frame parameters and vertical rates (average differences on the order of 0.3 mm/yr) across their global network, even as horizontal velocities remained in near-perfect agreement [12]. These studies suggest that the vertical component is especially sensitive to method nuances and underscores the importance of rigorous modeling when comparing solutions.

Another critical factor for reliable velocity estimation is the treatment of time-series noise. GNSS position residuals exhibit temporally correlated noise (power-law or flicker noise) rather than purely white noise, and ignoring this correlation can underestimate velocity uncertainties or even subtly bias the velocity estimates [5,16]. In an analysis of 200 European stations, Nistor et al. (2021) showed that using a flicker-noise model instead of a white-noise assumption increased the average vertical velocity uncertainty by 0.7 mm/yr; moreover, up to 10 stations showed >1 mm/yr differences in estimated vertical rate when using a robust trend estimator versus a conventional least-squares approach, reflecting the influence of noise model choice [4]. To obtain realistic uncertainties, modern GNSS analyses therefore incorporate stochastic noise modeling and seasonal signal estimation. Notably, the new ITRF2020 reference frame explicitly fits annual and semiannual terms to station time series and applies power-law noise models, which was found to reduce spurious vertical trends—omitting seasonal terms left vertical rates biased by 0.5–1 mm/yr at some sites [3]. Overall, adopting a consistent noise model (e.g., white + flicker noise) and accounting for offsets and periodic signals are essential steps to ensure that velocity uncertainties are comparable across software and that any inter-software differences are not artifacts of disparate noise assumptions.

In this context, the present study evaluates the consistency of GNSS-derived velocities obtained from multiple operational GNSS processing chains applied to a dense regional network in Southern Italy. The aim is not to benchmark software packages under strictly homogenized processing conditions, but to evaluate whether independently generated operational GNSS solutions produce mutually consistent long-term velocities suitable for regional geodynamic applications. We compare four solutions spanning 2017–2024: a classical double-difference network solution (using the Bernese 5.4 GNSS Software) and three precise point positioning solutions with ambiguity resolution (Bernese PPP-AR, the open-source PRIDE PPP-AR software, and the Nevada Geodetic Laboratory's PPP-AR pipeline using GipsyX). The selected software packages represent mature and widely used scientific or operational approaches for high-precision GNSS processing, consistent with recent comparative studies of PPP processing tools and services [17]. The daily coordinate series preserve the realistic differences among the processing chains, while the subsequent velocity estimation is performed with a common HectorP workflow, including automated offset detection and a combined white + flicker-like stochastic model [16,18]. By comparing the PPP-AR results with the Bernese DD reference solution, we assess inter-solution differences in each velocity component (with particular attention to any vertical offsets) and evaluate the consistency of current operational GNSS velocity products. The findings provide insight into the level of agreement that can be achieved between differential and PPP-AR approaches and contribute to best practices for integrating multi-software GNSS results into a consistent framework for crustal motion analysis.

2. Materials and Methods

2.1. Station Selection

All GNSS stations used in this study were selected from the European Plate Observing System (EPOS) GNSS Data Gateway [19], which provides access to standardized station metadata and RINEX data from numerous European GNSS networks. The station metadata (including installation dates, coordinates, and network affiliations) were exported from the EPOS Data Gateway and filtered through an automated Python 3.13 workflow. The selection process identified a high-quality subset of stations with reliable data records, as outlined in the following steps:

- **Installation date cutoff:** We first retained only stations that were installed and operational before 1 January 2022. This ensured each station had the potential for several years of data (at least through 2022–2024) and excluded recently installed sites with short or incomplete time series.
- **Geographic bounding box:** Next, stations were filtered by location to include only those within 36.0–40.0° N latitude and 8.0–18.0° E longitude. This spatial criterion focuses the network on the study region.
- **Data-availability assessment:** For each candidate station, we programmatically retrieved the metadata listing all daily RINEX observation files available for 2017–2024. From these records, we counted the number of days with at least one RINEX file and expressed this as a percentage of the total 2922 days in the eight-year window. Stations were ranked by their overall data coverage, and any site with <30% data availability was discarded.
- **Final selection:** Stations satisfying all of the above filters were retained for the time-series analysis.
- **Reference-frame strengthening:** To strengthen the regional reference frame, we added a set of IGS "core" stations that lie just outside the geographic window but provide long, stable records and tie the network to the global frame.
- **Network composition:** The final dataset therefore comprises 79 GNSS stations: 22 international sites belonging to the EUREF Permanent Network (EPN) and/or the IGS, and 57 national RING network [20] (Rete Integrata Nazionale GPS) stations [19].

A visual summary of the resulting network is presented in Figure 1, where the 57 RING stations [20] are plotted as blue circles and the 22 EPN/IGS core sites as red triangles. This combination of globally distributed reference sites and dense regional stations maximizes network stability and spatial resolution while maintaining high data completeness. The station-selection stage was based on metadata, observation availability, and network geometry; it was not intended as a homogenized raw-observation quality-control analysis. Indicators such as multipath, signal-to-noise ratio, cycle-slip rate, and observable integrity are handled internally by each processing chain, while the final screening in this study was applied at the time-series and velocity-comparison level.

All filtering and data extraction steps were carried out in a fully automated Python 3.13 workflow. The workflow utilized EPOS web APIs to retrieve station metadata (including IGS-style site log files) and to query daily file availability, thereby eliminating manual data collection and ensuring reproducibility. We emphasize that the EPOS GNSS Data Gateway aggregates data from many national and regional networks under an open data policy. All accessed GNSS data are distributed under a Creative Commons Attribution 4.0 (CC-BY) license, which guarantees open access and proper attribution to the original data providers [21].

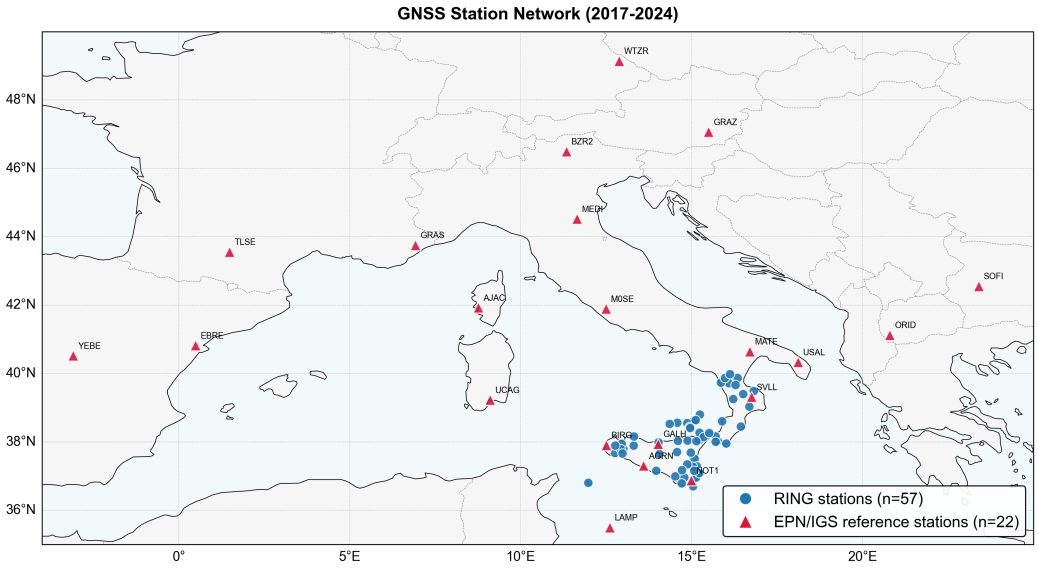

Figure 1. Location of the 79 GNSS stations analysed in this study. Blue circles correspond to the 57 Italian RING stations; red triangles indicate the 22 EPN/IGS reference sites that reinforce the regional tie to the global reference frame. The map shows the geographic distribution across Southern Italy (12.5–18.0° E, 36.0–41.0° N) with natural earth coastlines and national boundaries.

2.2. GNSS Data Processing Strategies

In this study, four different GNSS data processing strategies were employed to generate daily coordinate time series for each station. These include a classical network solution (double-differencing) and three precise point positioning solutions with ambiguity resolution (PPP-AR). Bernese DD was selected as an established scientific network-processing strategy and used as the reference solution; Bernese PPP-AR was included to compare DD and PPP-AR modes within the same software environment; PRIDE PPP-AR was selected as a modern open-source scientific PPP-AR implementation; and NGL/GipsyX was included because it is one of the most widely used public operational GNSS time-series products. The main configuration elements are summarized in Table 1, and the individual strategies are described in the following subsections. Because the PPP products considered here are daily 24 h static solutions, this comparison was not designed to isolate convergence-time or short-session benefits of additional constellations. Instead, constellation choice is treated as one element of each documented operational processing chain.

Table 1. Summary of the main processing-configuration elements used for the four GNSS coordinate solutions.

Parameter	Bernese DD	Bernese PPP-AR	PRIDE PPP-AR	Nevada/NGL GipsyX
Processing role	Reference network DD solution	Independent PPP-AR solution	Independent PPP-AR solution	Public operational PPP-AR time series
Software/version	Bernese GNSS Software v5.4	Bernese GNSS Software v5.4	PRIDE PPP-AR v3.0	JPL GipsyX v2.3 via NGL
Session/mode	Daily 24 h static network solution	Daily 24 h static PPP	Daily 24 h static PPP	Daily coordinate time series from NGL
Estimation framework	Least-squares normal-equation network adjustment	Station-wise PPP least squares/normal equations	PRIDE least-squares estimator with residual diagnosis and AR module	Daily Kalman-filter PPP processing as documented by NGL
Constellation	GPS-only	GNSS	GNSS	GPS-only
Products	CODE final products	CODE final products and OSB	CODE final products	JPL final IGS20 orbit/clock/WLPB products
Elevation cutoff	3°	7°	7°	7°

Table 1. *Cont.*

Parameter	Bernese DD	Bernese PPP-AR	PRIDE PPP-AR	Nevada/NGL GipsyX
Observation weighting	0.001 m; $1/\cos(Z)$ weighting	0.001 m; $1/\cos(Z)$ weighting	code noise 0.30 m; carrier-phase prior 0.01 cycles; variance scaled by $(1/(2\sin e))^2$ below 30°	LC 0.01 m, PC 1 m; $\sigma^2 = 1/\sin(e)$
Troposphere	DRY_GPT3; WET_GMF3; Chen–Herring gradients; 2 h ZD spacing; 24 h gradients	DRY_VMF3; WET_VMF3; Chen–Herring gradients; 1 h ZD spacing; 24 h gradients	Saastamoinen dry/wet a priori; VMF1 mapping; residual ZTD random walk; gradients piece-wise constants	VMF1 wet/dry a priori; ZD and gradients estimated as random walks every 5 min
Tidal/loading corrections	FES2022b OTL through BLQ; Ray–Ponte S1/S2; solid Earth tides IERS 2000; no atm./ocean/hydrol. NTL	FES2022b OTL through BLQ; Ray–Ponte S1/S2; solid Earth tides IERS 2000; no atm./ocean/hydrol. NTL	IERS 2003 solid Earth tides; OTL using the PRIDE oceanload coefficient table, based on FES2004; no atmospheric tidal, atm./ocean/hydrol. NTL	IERS 2010 solid Earth and pole tides; permanent tide retained; FES2004 OTL; ocean pole tide; no atm./ocean/hydrol. NTL
Reference frame	ITRF2020/IGS20	ITRF2020/IGS20 after ADDNEQ2 framing	ITRF2020/IGS20	IGS20 public NGL product
Ambiguity resolution	Double-difference ambiguity resolution	Bernese PPPIAR, SIGMA search	Rounding-based ambiguity resolution	JPL WLPB PPP-AR

2.2.1. Bernese GNSS Software (Double Difference)

The Bernese GNSS Software (v5.4) was used to generate a traditional double-difference network solution, which served as the reference solution for comparing all PPP-AR strategies. The densification network consisted of GNSS stations from the RING network located in Southern Italy, processed together with a set of long-term EPN reference sites. Station positions were estimated within the latest realization of the International Terrestrial Reference Frame (ITRF2020) [3]. The stations of the densification network were set to remain free to move within the reference frame defined by the reference network. The geodetic datum was established using a minimum-constraint approach, imposing a no-net translation (NNT) condition on the reference network with respect to ITRF2020 when solving the daily normal equations for station coordinates and tropospheric parameters. The processing utilized CODE final orbit and Earth rotation parameters. Ionospheric effects were mitigated through the ionosphere-free (L3) linear combination for first-order delays, while higher-order ionospheric terms were corrected using CODE global ionosphere maps (GIMs). Ocean tide loading was applied following the FES2022b model [22], atmospheric tidal loading (S1/S2) followed Ray and Ponte [23], and solid Earth and pole tide corrections were modeled following the IERS conventions [24]. Non-periodic atmospheric pressure loading, non-tidal ocean loading, and hydrological loading were not activated. An elevation cutoff of 3° was adopted to maximize satellite geometry and observation redundancy in the long-session network solution, together with elevation-dependent weighting and site-specific tropospheric parameter estimation. This analysis relied solely on GPS observations, enabling robust integer ambiguity resolution across the network baselines. Daily station coordinates were extracted and exported as time series for velocity analysis.

2.2.2. Bernese GNSS Software (PPP-AR)

The Bernese GNSS Software (v5.4) was configured in Precise Point Positioning mode with Ambiguity Resolution (PPP-AR), following a two-stage workflow consisting of float parameter estimation and subsequent integer ambiguity resolution. Daily RINEX observation files for all 79 stations were processed in 24 h static sessions spanning 2017–2024 using the Bernese Processing Engine (BPE). The processing utilized CODE final orbit and clock products, with observable-specific biases (OSB) provided in Bias-SINEX format and converted to Bernese OSB format for ambiguity resolution. Multi-GNSS observations from GPS, GLONASS, Galileo, and BeiDou satellites were combined into ionosphere-free (L3) linear combinations with an elevation cutoff of 7°, selected because undifferenced PPP

processing is more sensitive to low-elevation multipath and tropospheric mismodeling. Tropospheric zenith wet delays were estimated as piecewise-linear parameters at 1-h intervals using the Vienna Mapping Function 3 (VMF3) [25], while horizontal tropospheric gradients were modeled using the Chen–Herring formulation [26] with daily resolution. Antenna phase center variations were applied using IGS ANTEX calibration files. Ocean tide loading was applied following the FES2022b model [22], atmospheric tidal loading (S1/S2) followed Ray and Ponte [23], and solid Earth and pole tide corrections were modeled following the IERS conventions [24]. Non-periodic atmospheric pressure loading, non-tidal ocean loading, and hydrological loading were not activated. Integer ambiguity resolution was performed using the PPPIAR module with the SIGMA search algorithm. The Bernese PPP-AR coordinates used in this study were aligned to the ITRF2020/IGS20 reference frame through a normal-equation reference-frame stabilization step prior to generation of the daily coordinate time series for velocity analysis.

2.2.3. PRIDE PPP-AR

The PRIDE PPP-AR (v3.0) software [10] was used to generate an independent undifferenced PPP solution with integer ambiguity resolution. Daily 24 h static GNSS sessions spanning 2017–2024 were processed using ionosphere-free linear combinations and CODE final precise products, with a 7° elevation cutoff. The PRIDE processing used an elevation-dependent weighting scheme with pseudorange observation noise of 0.30 m, a carrier-phase prior constraint of 0.01 cycles, and variance scaled by $(1/(2\sin e))^2$ for elevations below 30°, while observations above 30° were left unscaled.

A priori tropospheric delays were modeled using the Saastamoinen dry/wet model with VMF1 mapping. Residual zenith tropospheric delay was estimated as a stochastic random-walk parameter using the standard PRIDE process noise of 0.0004 m $\sqrt{\mathrm{s}^{-1}}$, and horizontal gradients were estimated as piecewise constants with 720 min spacing and 0.002 m process noise. Solid Earth tides followed IERS Conventions 2003. Ocean tide loading was applied using the PRIDE oceanload coefficient table, based on FES2004 coefficients in the standard workflow; atmospheric tidal loading, non-tidal atmospheric pressure loading, non-tidal ocean loading, and hydrological loading were not applied. Integer ambiguities were resolved for the 24 h solutions using the rounding/bootstrapping-based ambiguity-resolution strategy implemented in PRIDE. Station coordinates were estimated in the ITRF2020/IGS20 reference frame and exported as daily time series for subsequent velocity analysis. Consequently, the PRIDE comparison is interpreted as an independent operational PPP-AR processing chain rather than as a strictly single-variable software experiment.

2.2.4. Nevada Geodetic Laboratory (NGL) Time Series

The Nevada Geodetic Laboratory (NGL) at the University of Nevada, Reno generates daily GNSS coordinate time series using JPL's GipsyX software (v2.3) in precise point positioning with ambiguity-resolution (PPP-AR) mode. This global processing covers over 13,000 stations, with results provided as daily east, north, and up displacements in the IGS20 reference frame (`tenv` files) [27]. For this study, we downloaded NGL's IGS20 `tenv` time series for all 79 selected stations and converted them to HectorP-required format for a consistent post-processing workflow.

The NGL IGS20 processing strategy used here is GPS-only after removal of non-GPS observations. It adopts JPL's final IGS20 satellite orbits and clocks and resolves integer ambiguities using JPL's widelane-phase bias (WLPB) products. The documented observation weights are 0.01 m for the ionosphere-free phase combination and 1 m for the code combination, with elevation weighting proportional to $1/\sin(e)$. Tropospheric

wet and dry a priori delays are taken from VMF1 grids, and zenith delays and horizontal gradients are estimated as random-walk parameters every 5 min. First-order ionospheric effects are removed by forming ionosphere-free observations, and second-order ionospheric corrections are applied using JPL's global IONEX maps together with the IGRF12 magnetic field. Periodic tidal displacements are modeled following IERS 2010 conventions [24], including solid Earth and pole tides, FES2004 ocean tide loading, a semiannual equilibrium ocean tide, and ocean pole tide loading. Permanent solid Earth tides are not removed, and non-tidal atmospheric pressure, ocean bottom pressure, and hydrological loading corrections are not applied. Station coordinates are estimated with a daily Kalman-filter PPP strategy and aligned to the IGS20 terrestrial reference frame [27].

2.3. GNSS Time Series Analysis

Once daily coordinate time series were obtained from each GNSS processing strategy (Bernese double-differencing, Bernese PPP-AR, PRIDE PPP-AR), a consistent post-processing workflow was applied to estimate station velocities and quantify their uncertainties. For cross-validation, we also included time series from an independent repository [27,28] over the same period (1 January 2017 to 31 December 2024). All station series were truncated to this common eight-year interval to ensure comparability. Each series was converted to the HectorP `.MOM` format required by the HectorP time-series analysis software [18], standardizing the time units to days (with reference epoch MJD 0) and position units to millimeters. This format conversion preserved data gaps and handled any duplicate entries so that the subsequent analysis accurately reflected the original daily solutions.

We employed HectorP (v0.1.12) to perform a three-step maximum-likelihood estimation on each coordinate component. HectorP was chosen because it allows simultaneous estimation of deterministic trends, seasonal signals, offsets, and temporally correlated noise through maximum-likelihood estimation [16,18]. In this study, the same HectorP workflow was applied to all independently generated coordinate solutions to ensure methodological consistency during the velocity-estimation stage. The overall functional model for each position component comprised: a reference offset (intercept), a linear velocity, periodic oscillations (annual and semiannual sinusoidal terms), and step discontinuities at any detected offset epochs. Crucially, the noise in the time series was modeled as a combination of white noise (temporally uncorrelated) and power-law noise (flicker-like noise, approximated here as a Generalized Gauss–Markov process) [16]. This white+GGM noise model reflects the typical error spectrum of geodetic position time series, providing more realistic velocity uncertainties than would be obtained under a white-noise-only assumption [16]. All time series, regardless of processing method, were analyzed using the same model assumptions and parameters to ensure a uniform comparison of their results.

Outlier Removal and Seasonal Adjustment: The first step of the analysis was an automated identification and removal of statistical outliers in the time series. We employed a single-pass outlier detection criterion based on the interquartile range ($3 \times$ IQR). To avoid flagging legitimate geophysical signals as outliers, we simultaneously modeled and removed the dominant seasonal variations before outlier testing. Specifically, sinusoidal terms with periods of 1 year (365.25 days) and 0.5 years (182.625 days) were estimated and subtracted during this stage. This yielded "cleaned" position series free of gross errors, which were then carried forward to the next steps. On average, only a few points per station (often <1% of the data) were removed as outliers, reflecting the generally high quality of the daily GNSS solutions.

Offset Detection with Correlated Noise Modeling: In the second step, we applied HectorP's automatic offset detection algorithm to the cleaned series [18]. This procedure

seeks to identify any unknown temporal discontinuities (step changes) in the position history, which could arise from instrumentation changes, seismic events, or other abrupt shifts. The analysis was performed under a full stochastic noise model that includes both white and flicker noise components, since even subtle offsets can be obscured by temporal correlations in the data. Using a generalized Gauss–Markov (GGM) stochastic model with the configured GGM spectral index, HectorP computes the full covariance of the observations [18]. Candidate offsets are tested one by one at each possible epoch: the software introduces a step function at that date into the model and evaluates the improvement in log-likelihood. An offset is accepted as significant when HectorP's built-in log-likelihood gain criterion is met. All three components (E, N, U) are analyzed in this manner, with offsets detected independently for each component of the cleaned series. Detected offsets are then incorporated into the model, and the search repeats to find the next candidate, until no additional significant offsets remain. Importantly, by using a realistic correlated-noise model during detection, we reduce the risk of flagging false offsets that could arise from colored noise fluctuations [18].

It is worth noting that the offset detection algorithm can become unstable for time series with extremely large data gaps. The full covariance approach may fail to converge or yield singular matrices when more than about 60% of the data are missing, as there is insufficient information to estimate the noise parameters reliably. For these special cases, a simplified white-noise-only model was used temporarily during the offset-search step as a pragmatic workaround. However, the only station exceeding the 60% gap threshold was MPAZ, and this station was subsequently excluded during the Bland–Altman and residual-RMS screening. Consequently, no high-gap or pure-white-noise-only station/component series enters the final 69-station intercomparison presented in this study.

Trend Estimation and Uncertainty Assessment: In the final step, we estimated the linear trend (velocity) for each station and component by fitting the full model—including the linear term, seasonal signals, and any identified offsets—using maximum likelihood estimation. The noise parameters (white-noise amplitude and GGM amplitude) were re-estimated from the residuals in this stage to refine the uncertainty assessment of the trend. The result for each station component is an optimized velocity estimate (in mm yr^{-1}) accompanied by a 1σ uncertainty that reflects the power-law noise spectrum of the residuals [16]. Typically, the presence of flicker noise inflates the velocity uncertainty compared with a naive white-noise assumption; by capturing this effect, our analysis provides more conservative and realistic error bars on the computed velocities. Along with velocities, the final solution yields the amplitudes and phases of the annual and semiannual signals and the magnitudes of any detected offsets, as well as goodness-of-fit metrics. We extracted these parameters for all processing solutions into summary tables and plots (e.g., residual RMS, noise amplitudes, etc.) to compare the fidelity and precision of each solution type. Here we emphasize that the same rigorous analysis protocol was applied uniformly to all solutions, ensuring that the velocity-estimation stage itself is consistent across solutions, so that remaining differences can be interpreted in relation to the input daily coordinate series and their respective processing-chain characteristics.

Overall, this time-series analysis approach–leveraging HectorP's advanced noise modeling and iterative outlier/offset detection–provides a robust framework for GNSS velocity estimation. By accounting for temporally correlated noise and transient events, we obtain velocity estimates with realistic uncertainty bounds [16,18]. Applying the same HectorP velocity-estimation workflow to all independently generated coordinate series allows the final velocity-estimation stage to be evaluated under a common analysis framework.

2.4. Outlier Detection and Data Quality Screening

After estimating station velocities from all four processing strategies, we applied a Bland–Altman method-comparison analysis [29,30] to identify stations with anomalous inter-solution velocity differences that could bias the statistical comparison. The analysis was performed separately for each PPP solution relative to the Bernese double-difference (DD) reference—namely Bernese PPP-AR versus DD, PRIDE PPP-AR versus DD, and Nevada/NGL versus DD—for each coordinate component (E, N, U). For each comparison, station-wise velocity differences were computed as

$$d_i = v_{\mathrm{DD},i} - v_{\mathrm{PPP},i},$$

and the 95% limits of agreement (LoA) were defined as

$$\mathrm{LoA} = \bar{d} \pm 1.96\,\sigma_d,$$

where $\bar{d}$ is the mean difference and σ_d is the standard deviation of the differences across all stations. Stations falling outside these limits were flagged as candidate outliers. The resulting statistics for each comparison and component are summarised in Table 2.

Because a purely statistical union of all candidate outliers may also capture software-specific sensitivities rather than genuinely problematic stations, candidate stations were subsequently classified using additional geodetic quality criteria, namely (i) the persistence of anomalous behaviour across multiple solutions and/or coordinate components, and (ii) the residual RMS of the corresponding time series relative to the network median (1.67 mm for Bernese DD). This combined assessment was used to distinguish stations with consistently poor behaviour from stations affected only by isolated method-dependent discrepancies.

Using this strategy, 10 stations were excluded from the main comparison dataset: CAVT, CLTA, CRJA, ESLN, GBLM, HVZN, LI3D, MMGO, MPAZ, and MTGR. The station-level evidence supporting each decision is provided in Table 3. The resulting main dataset therefore comprises **69 stations** (87.3% of the original network).

Table 2. Number of stations flagged outside the 95% limits of agreement for each PPP-vs-DD comparison and coordinate component (79 stations total). n_{flag}: number of flagged stations.

Comparison	Comp.	n_{flag}
Bernese PPP vs. DD	E	4
	N	5
	U	7
PRIDE vs. DD	E	5
	N	5
	U	4
Nevada/NGL vs. DD	E	3
	N	1
	U	4

The excluded stations do not represent a single failure mode. In general, they are characterized by combinations of shorter usable records, larger data gaps, elevated residual RMS values or velocity uncertainties, and larger inter-solution velocity discrepancies, particularly in the vertical component. Several excluded stations also exhibit more complex station histories involving receiver, antenna, or eccentricity changes. These metadata changes were included in the Bernese processing and are not interpreted here as unmodeled corrections, but rather as indicators of potentially more complex discontinuity behaviour. Raw multipath, SNR, and cycle-slip diagnostics were not available in a homogeneous form

for all processing chains and were therefore not used to assign unique physical causes to individual station exclusions.

Table 3. Candidate outlier stations identified by Bland–Altman screening, supporting residual RMS diagnostics, and final classification. RMS_{DD}: mean residual RMS of the Bernese DD time series averaged over E, N, and U; network median = 1.67 mm.

Station	n_{flags}	RMS_{DD} (mm)	Decision
CAVT	5	2.60	Exclude
CLTA	1	5.10	Exclude
CRJA	3	2.40	Exclude
ESLN	2	17.20	Exclude
GBLM	2	3.00	Exclude
HVZN	2	5.30	Exclude
LI3D	3	2.70	Exclude
MMGO	3	1.70	Exclude
MPAZ	5	2.30	Exclude
MTGR	3	2.00	Exclude
HAGA	1	2.30	Borderline
HAVL	2	2.60	Borderline
HSRS	2	2.40	Borderline
MILA	2	2.10	Borderline
MSRU	1	2.20	Borderline
MFNL	1	2.60	Borderline

3. Results

3.1. Overview of the Clean Dataset

This study assessed the agreement of three PPP solutions—PRIDE-PPP, Nevada/NGL, and Bernese_PPP—with Bernese differential (double-difference) solution velocities for 69 GNSS stations. Following the outlier detection strategy described in Section 2.4, 10 stations were excluded, resulting in a clean dataset with 87.3% retention rate. The comparisons are organized by coordinate component (E, N, U) and horizontal magnitude.

Table 4 summarises the mean residual root mean square (RMS) of the daily position time series after outlier removal and seasonal adjustment, computed by component for each processing strategy.

Table 4. Average residual RMS (mm) by component and processing method for the cleaned dataset of 69 stations.

Component	Bernese_DD	PRIDE-PPP	Nevada/NGL	Bernese_PPP
E	1.46	1.89	1.73	3.52
N	1.84	2.36	2.15	3.01
U	4.88	5.80	5.59	7.33

3.2. Velocity Consistency and Distributions

Velocity distributions for each component and processing method are summarised in Figure 2, which presents box plots of the E, N and U velocities for all four processing strategies. The horizontal components have similar medians and interquartile ranges across methods, whereas the vertical component exhibits larger dispersion.

Mean differences, standard deviation and RMS values for each PPP method relative to the Bernese differential solution are summarised in Table 5. For the E component, all PPP solutions have sub-millimetric mean differences and RMS values below 0.6 mm yr^{-1}. For the N component, RMS values remain below 0.8 mm yr^{-1}. The vertical component

shows larger biases and RMS values, ranging from about 0.7 to 1.4 mm yr^{-1} across the PPP methods.

Table 5. Mean, standard deviation and RMS of velocity differences (mm yr^{-1}) between Bernese differential and each PPP solution for the E, N and U components. Negative means indicate the PPP solution is faster than the differential solution, positive values indicate the reverse.

Component	PPP Solution	Mean	SD	RMS
E	PRIDE-PPP	−0.17	0.27	0.32
	Nevada/NGL	−0.20	0.53	0.56
	Bernese_PPP	−0.02	0.31	0.31
N	PRIDE-PPP	0.06	0.58	0.58
	Nevada/NGL	−0.05	0.44	0.44
	Bernese_PPP	0.51	0.61	0.79
U	PRIDE-PPP	−0.35	1.28	1.32
	Nevada/NGL	0.19	0.68	0.70
	Bernese_PPP	1.05	0.86	1.35

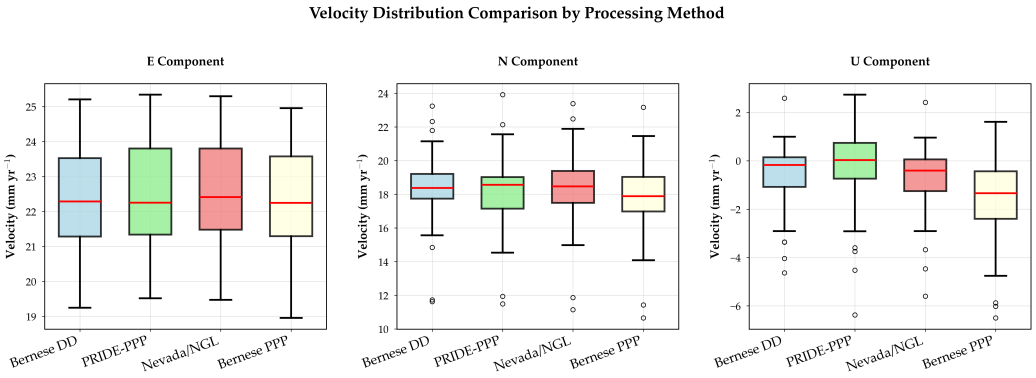

Figure 2. Box plots of station velocities (mm yr^{-1}) for the East (E), North (N), and Up (U) components across the four processing strategies (Bernese_DD, PRIDE-PPP, Nevada/NGL, and Bernese_PPP). Each box represents the interquartile range (IQR) of the 69-station velocity distribution, with the median shown as a horizontal line; whiskers extend to 1.5 × IQR, and individual outliers are plotted as dots. The horizontal components show similar medians and compact distributions across all methods, consistent with inter-solution agreement, while the vertical component exhibits larger spread.

3.3. Correlation Across Station Velocity Estimates

Horizontal components (E and N) display strong correlations computed across the station velocity estimates obtained from the PPP solutions and the Bernese DD reference. As shown in Table 6, correlation coefficients for the E component are between 0.94 and 0.98, and RMS differences are below 0.6 mm yr^{-1}. The N component shows similar behaviour, with correlation coefficients between 0.95 and 0.98 and RMS differences up to 0.79 mm yr^{-1}. The U component exhibits greater variability: correlation coefficients range from 0.59 (PRIDE-PPP) to 0.86 (Nevada/NGL), and the corresponding RMS differences span 0.7–1.4 mm yr^{-1}.

The correlations reported in Table 6 are computed across the 69 retained station velocity estimates, rather than from the daily coordinate time series themselves. Each processing solution was analyzed independently using the same HectorP workflow. The white + GGM stochastic model was used separately for each time series to estimate velocities and their uncertainties. Therefore, the reported R values describe the coherence of the long-term regional velocity field across the station network. Residual RMS values and velocity-difference statistics remain complementary diagnostics, because daily coordinate scatter

can differ substantially among solutions even when their long-term horizontal velocity fields are coherent.

Table 6. Correlation (R) computed across station velocity estimates and RMS velocity difference (mm yr^{-1}) for each PPP solution relative to the Bernese differential reference, by component.

Component	Pair (Bernese_DD)	R	RMS
E	PRIDE-PPP	0.98	0.32
	Nevada/NGL	0.94	0.56
	Bernese_PPP	0.98	0.31
N	PRIDE-PPP	0.96	0.58
	Nevada/NGL	0.98	0.44
	Bernese_PPP	0.95	0.79
U	PRIDE-PPP	0.59	1.32
	Nevada/NGL	0.86	0.70
	Bernese_PPP	0.85	1.35

Figure 3 provides a graphical representation of the inter-solution agreement by plotting PPP-derived station velocities against the Bernese DD reference solution for the East (E), North (N), and Up (U) components. The horizontal velocity estimates exhibit a coherent station–network relationship, with most stations clustered closely around the 1:1 identity line, consistent with the correlations reported in Table 6. In contrast, the vertical component shows a noticeably larger dispersion around the identity line, reflecting the lower correlation coefficients and larger RMS differences observed for U.

It is also noticeable that, although PRIDE-PPP and Bernese_PPP show similar RMS values relative to the Bernese DD solution, Bernese_PPP exhibits a higher correlation with the reference vertical velocity field than PRIDE-PPP, with points distributed more closely around the 1:1 line. At the same time, PRIDE-PPP shows a smaller mean bias but lower correlation, indicating larger station-dependent dispersion in the vertical velocity estimates.

3.4. Precision and Uncertainty Assessment

Time-series precision was assessed using the average residual RMS values listed in Table 4. For the E component, RMS values range from 1.46 mm (Bernese differential) to 3.52 mm (Bernese_PPP). In the N component, the values range from 1.84 mm to 3.01 mm, and in the U component from 4.88 mm to 7.33 mm. Among the PPP methods, Nevada/NGL has the lowest RMS values, whereas Bernese_PPP shows higher RMS values across components. These residual RMS differences indicate that the daily coordinate series entering the HectorP velocity-estimation stage retain solution-dependent scatter.

Formal precision comes from HectorP's 1 σ velocity uncertainties (σ_v). Table 7 lists the mean σ_v for each component and method. Horizontal uncertainties are approximately 0.15–0.44 mm yr^{-1} and vertical uncertainties are around 0.37–0.52 mm yr^{-1}.

Figure 4 illustrates the distribution of HectorP-derived 1σ velocity uncertainties (σ_v) for each processing strategy and coordinate component. The horizontal components (E and N) exhibit relatively small uncertainties across all solutions, generally below 0.5 mm yr^{-1}. In contrast, the vertical component shows systematically larger uncertainties, reflecting the greater sensitivity of vertical velocity estimates to residual noise and modelling errors in GNSS time series. Among the PPP implementations, Nevada/NGL and PRIDE-PPP produce comparable uncertainty levels, while Bernese_PPP tends to exhibit slightly larger formal uncertainties, particularly in the E component. These patterns are consistent with the mean values reported in Table 7 and highlight the overall robustness of the horizontal velocity estimates compared with the vertical component.

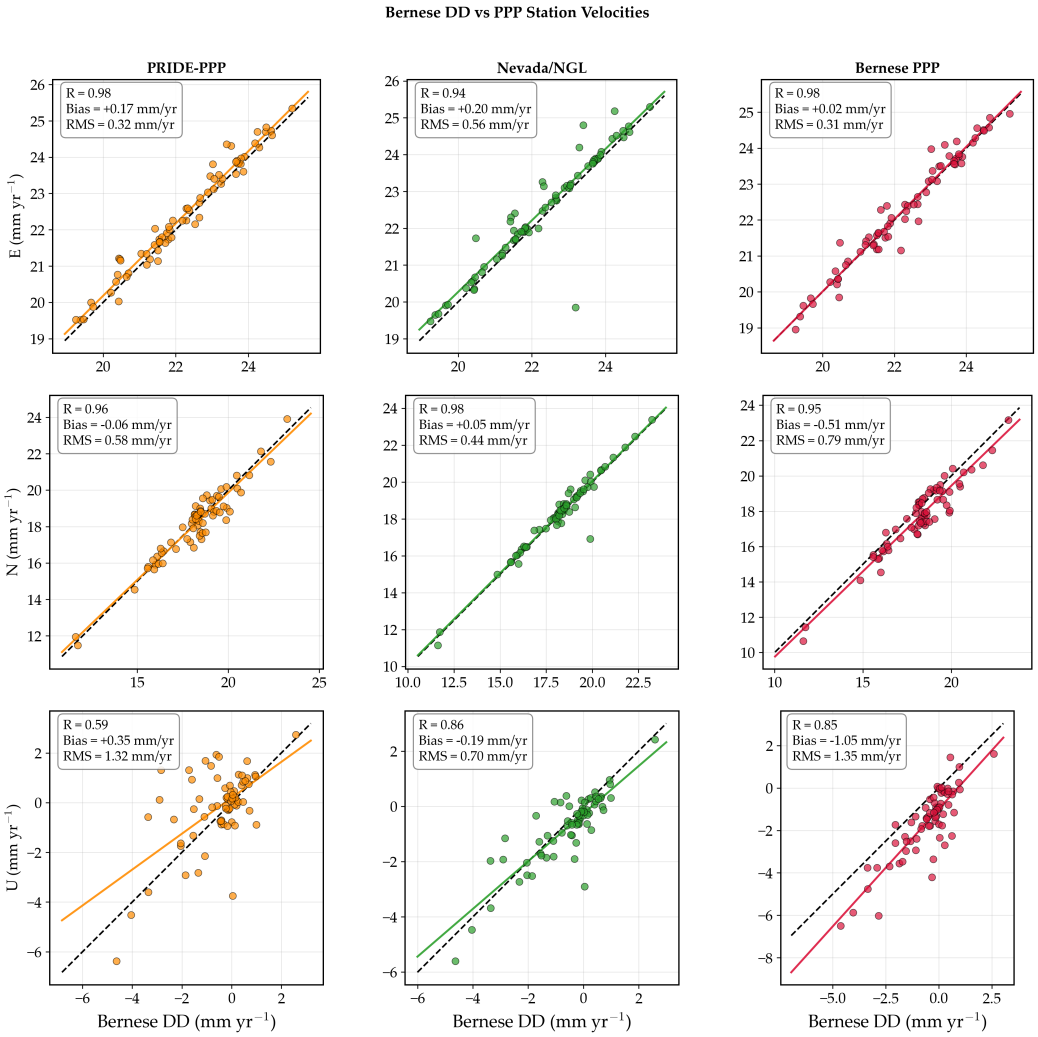

Figure 3. Scatter plots comparing station velocities derived from the PPP solutions (PRIDE-PPP, Nevada/NGL, and Bernese_PPP) with the Bernese DD reference solution for the East (E), North (N), and Up (U) components. Each panel shows the PPP-derived velocities versus the corresponding Bernese DD velocities for the 69 stations retained after outlier screening. The dashed line represents the 1:1 identity relationship, while the coloured line indicates the fitted regression. Insets report the correlation coefficient (R), mean bias, and RMS difference for each comparison.

Table 7. Mean 1 σ velocity uncertainties (σ_v, mm yr^{-1}) derived from HectorP for each component and method.

Component	Bernese_DD	PRIDE-PPP	Nevada/NGL	Bernese_PPP
E	0.17	0.20	0.19	0.44
N	0.15	0.24	0.21	0.27
U	0.37	0.46	0.46	0.52

3.5. Horizontal Velocity Magnitude Comparison

Horizontal velocity magnitudes derived from the PPP solutions agree closely with the differential reference (Table 8). All PPP methods achieve correlation coefficients R $\geq$ 0.94 and RMS differences not exceeding 0.65 mm yr^{-1}. PRIDE-PPP has a mean difference of +0.09 mm yr^{-1}, Nevada/NGL +0.19 mm yr^{-1} and Bernese_PPP −0.29 mm yr^{-1}, with corresponding RMS values of 0.40, 0.65 and 0.55 mm yr^{-1}, respectively.

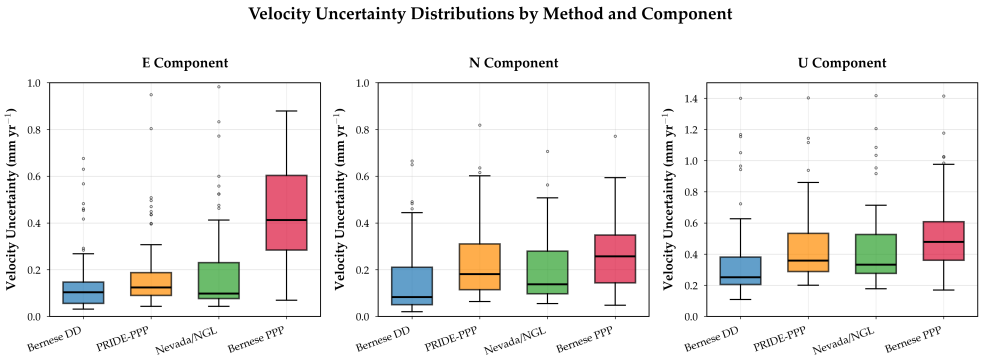

Figure 4. Distribution of HectorP-derived 1σ velocity uncertainties (σ_v, mm yr^{-1}) for the East (E), North (N), and Up (U) components across the four processing strategies (Bernese_DD, PRIDE-PPP, Nevada/NGL, and Bernese_PPP). Boxplots summarise the median, interquartile range, and outliers for the station-wise uncertainty estimates, allowing comparison of formal velocity precision between methods and coordinate components. The y-axis is limited to 1.0 mm yr^{-1} for E and N, and 1.5 mm yr^{-1} for U, to emphasise the central distribution.

Table 8. Statistics of horizontal velocity magnitude differences ($\sqrt{E^2 + N^2}$) between Bernese differential and each PPP solution. Bias, RMS and R values quantify systematic and random differences; N is the number of stations.

Method	N	Mean	Std	RMS	R
PRIDE-PPP	69	0.09	0.39	0.40	0.98
Nevada/NGL	69	0.19	0.63	0.65	0.94
Bernese_PPP	69	−0.29	0.46	0.55	0.96

All statistics in mm yr^{-1} except N and R.

Figure 5 provides a graphical comparison of the horizontal velocity magnitudes derived from each PPP solution relative to the Bernese DD reference. In all three cases, the station velocities cluster closely around the 1:1 identity line, indicating strong agreement in horizontal velocity magnitude between the PPP solutions and the differential processing.

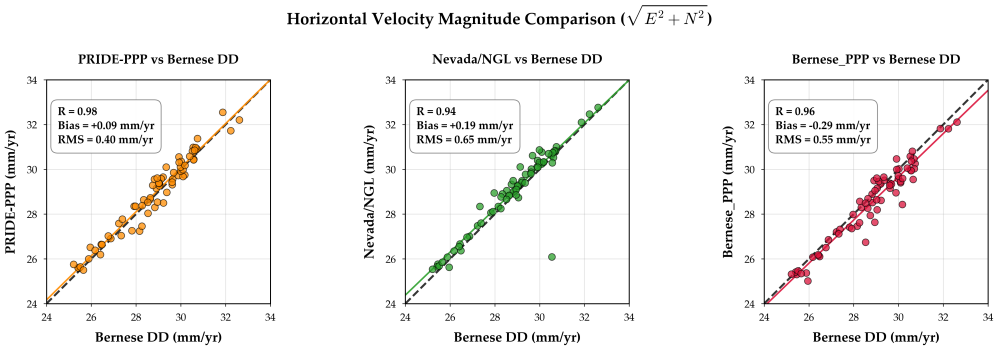

Figure 5. Comparison of horizontal velocity magnitudes ($\sqrt{E^2 + N^2}$, mm yr^{-1}) derived from the PPP solutions (PRIDE-PPP, Nevada/NGL, and Bernese_PPP) relative to the Bernese DD reference solution. Each panel shows the PPP-derived magnitude plotted against the corresponding Bernese DD value for the 69 stations retained after outlier screening. The dashed line represents the 1:1 identity relationship, while the coloured line indicates the fitted regression. Insets report the correlation coefficient (R) and RMS difference for each comparison.

3.6. Summary of Inter-Solution Agreement

The four-way comparison of GNSS velocity estimates across 69 retained stations shows very strong agreement in the horizontal components (E and N), with mean biases below 0.60 mm yr^{-1}, RMS differences below 0.85 mm yr^{-1} and correlations R $\geq$ 0.94 for all PPP solutions relative to the Bernese differential solution. Vertical velocities show greater

variability, with mean biases ranging from -0.35 mm yr^{-1} (PRIDE-PPP) to $+1.05$ mm yr^{-1} (Bernese_PPP) and correlations from 0.59 to 0.86. Nevada/NGL exhibits the highest vertical correlation (R = 0.86), while also showing the smallest mean vertical bias ($+0.19$ mm yr^{-1}). Horizontal magnitude analysis confirms sub-millimetric agreement (RMS ≤ 0.65 mm yr^{-1}) across all solutions.

3.7. Spatial Velocity Field Patterns

The spatial distribution of crustal velocities derived from all four processing strategies is presented in Figures 6 and 7. Figure 6 shows the horizontal velocity field for the 69-station network, with arrows color-coded by processing solution: Bernese DD (blue), Bernese PPP (red), Nevada/NGL (green), and PRIDE-PPP (orange). All four solutions are plotted simultaneously on the same map to facilitate direct visual comparison. The horizontal velocity field reveals the dominant NE-ward motion characteristic of the Adria microplate, with velocities ranging from 15 to 25 mm yr^{-1}. The strong spatial coherence is evident, with arrows from different solutions nearly overlapping at most stations, showing strong inter-solution agreement in the horizontal component.

To improve the readability of the vertical comparison, Figure 7 presents vertical velocity differences instead of four overlapping absolute vertical velocity maps. The plotted quantity is Bernese DD minus each PPP solution, consistent with Table 5. Positive values indicate that the Bernese DD vertical velocity exceeds the corresponding PPP estimate, whereas negative values indicate that the PPP vertical velocity is larger. The 69 stations shown represent the final dataset after removal of 10 outliers identified through the screening strategy described in Section 2.4.

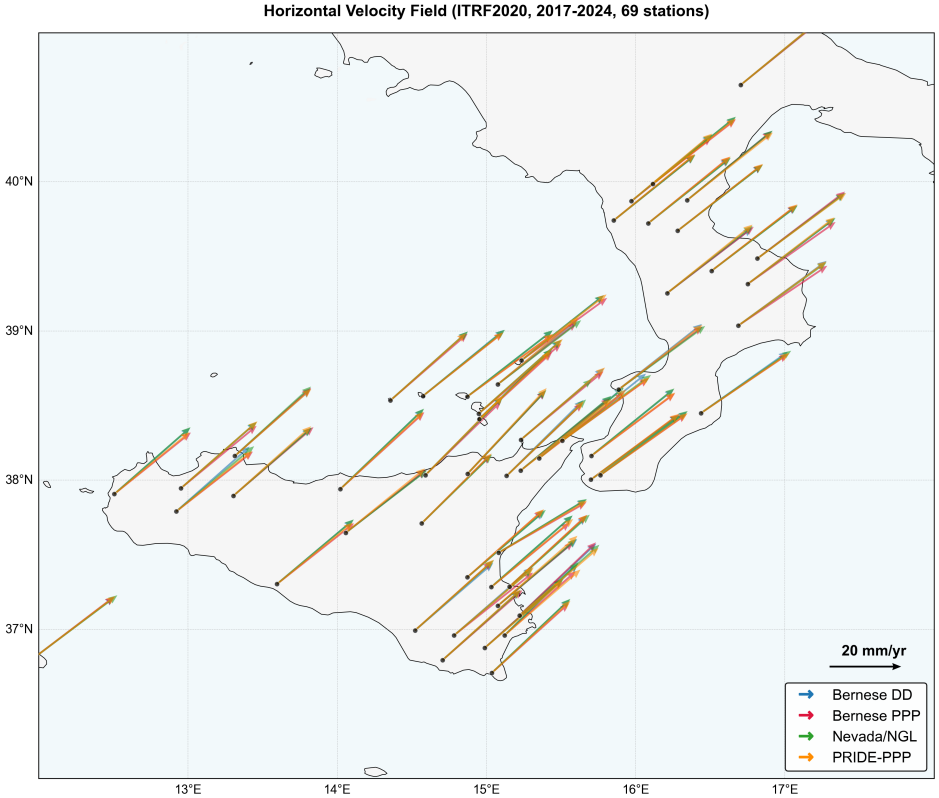

Figure 6. Geographic distribution of horizontal crustal velocities (ITRF2020, 2017–2024) for 69 GNSS stations across Southern Italy. Arrows indicate velocity magnitude and azimuth, color-coded by processing solution: Bernese DD (blue), Bernese PPP (red), Nevada/NGL (green), and PRIDE-PPP (orange). Reference arrow indicates 20 mm yr^{-1}. Station positions are marked with black circles. The close overlap of colored arrows illustrates strong inter-solution agreement in the horizontal component.

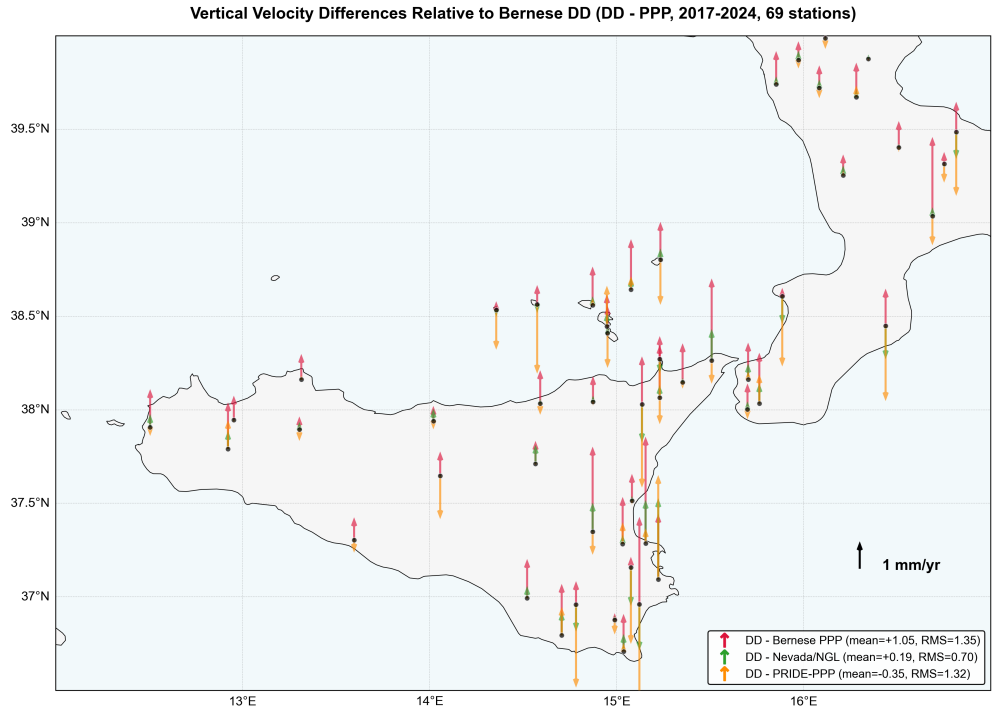

Figure 7. Geographic distribution of vertical velocity differences relative to the Bernese DD reference solution for the retained 69 stations. The plotted quantity is Bernese DD minus each PPP solution (DD–PPP), shown with colored vertical arrows for Bernese PPP-AR, Nevada/NGL, and PRIDE-PPP. Positive arrows indicate that the Bernese DD vertical rate is larger than the PPP rate; negative arrows indicate that the PPP rate is larger. Reference arrow indicates 1 mm yr^{-1}.

4. Discussion

The inter-comparison of GNSS velocity solutions shows strong horizontal consistency but notable vertical variability across processing strategies. In the horizontal components, all PPP-AR approaches produced velocity estimates highly consistent with the classical differential reference, with correlations of $R \geq 0.94$, RMS velocity differences below 0.85 mm yr^{-1}, and mean biases below 0.60 mm yr^{-1}. In this context, the correlation coefficients describe the coherence of the station–network velocity field, whereas the RMS differences and mean biases quantify the magnitude and systematic component of the inter-solution velocity differences. These findings indicate that, for the analyzed daily static velocity products, PPP-AR solutions provide horizontal velocity estimates strongly consistent with the network-constrained solution [14].

It is important to emphasize that harmonized processing settings would be required to isolate intrinsic software-algorithm performance. The present study instead considers independently generated operational GNSS solutions, each characterized by its own processing strategy, observation configuration, stochastic parameterization, ambiguity-resolution implementation, ancillary products, and geophysical modeling choices. Consequently, the observed inter-solution differences are interpreted as the cumulative effect of complete processing chains rather than as isolated software effects. The similarity between GPS-only and GNSS-inclusive horizontal velocity fields should therefore be interpreted within this daily-static, long-term velocity context. After convergence of 24 h static PPP solutions, the incremental effect of additional constellations on long-term velocities may be smaller than in short-session, kinematic, real-time, or obstructed-environment applications, where geometry, observation availability, and convergence time are more limiting. This does not imply that GPS-only and GNSS-inclusive processing are equivalent, or that multi-GNSS observations provide no benefit in other processing contexts.

Vertical velocities exhibit larger dispersion and systematic offsets between methods. This behavior is consistent with the well-known limitation that vertical velocity uncertainties are typically two to three times larger than horizontal components [2,4]. Despite an eight-year time span and rigorous noise modeling (Section 2.3), vertical scatter remains at the $\sim$1 mm yr^{-1} level, comparable to other recent inter-comparisons [14]. Bernese_PPP (R = 0.85) shows a systematic vertical offset relative to the DD reference and the largest vertical RMS difference (1.35 mm yr^{-1}), while PRIDE-PPP exhibits the weakest vertical correlation (R = 0.59) and substantial station-dependent scatter (RMS = 1.32 mm yr^{-1}). In contrast, the Nevada/NGL solution achieves the highest vertical correlation (R = 0.86), minimal DD-minus-PPP vertical mean difference ($+$0.19 mm yr^{-1}; Table 5), and the lowest time-series noise among the PPP products (Table 4).

The vertical differences likely reflect a combination of reference-frame realization, troposphere-height coupling, loading and tidal treatment, elevation weighting, observation-system differences, ambiguity-resolution implementation, precise products, and stochastic constraints. Precise-product differences may contribute because Bernese and PRIDE use CODE products, whereas NGL/GipsyX relies on JPL products. However, product choice alone cannot explain the results: Nevada/NGL uses a different product family from the Bernese DD reference but shows the closest Up agreement, while Bernese PPP-AR and PRIDE PPP-AR share the CODE product family yet still exhibit different vertical behavior. This indicates that the full processing strategy, rather than a single modeling choice, contributes to the residual vertical discrepancies.

Despite these vertical differences, the overall inter-solution agreement remains strong for practical regional geodynamic applications, especially in the horizontal components. A 1 mm yr^{-1} vertical difference is small for many tectonic applications, but not negligible for applications focused on vertical land motion or sea-level studies. The observed sub-millimetric horizontal agreement between independent operational solutions supports the practical maturity of PPP-AR for long-term horizontal velocity estimation, while the $\sim$1 mm yr^{-1} vertical differences indicate that vertical rates require explicit awareness of the adopted processing strategy.

Future work should include controlled reprocessing experiments in which the observation-system configuration, including GPS-only versus multi-GNSS processing, is explicitly tested while other processing settings are progressively homogenized. These settings should include precise products, elevation masks, loading and tropospheric models, stochastic constraints, ambiguity-resolution settings, and raw-observation quality-control metrics. Fixed/float ambiguity-control tests would further help separate constellation effects from ambiguity-resolution behaviour. Such tests would complement the operational comparison presented here by separating individual algorithmic effects from complete processing-chain variability.

5. Conclusions

This study analyzed an eight-year GNSS velocity dataset (2017–2024) from 79 stations, comparing a traditional double-difference (Bernese) solution with three precise point positioning strategies (Bernese PPP-AR, PRIDE-PPP, and NGL's GipsyX-based PPP). The objective was not to introduce a new GNSS processing algorithm but to test whether independently generated operational GNSS processing chains yield mutually consistent long-term velocities when analyzed with a common HectorP workflow. A Bland–Altman analysis flagged 10 stations ($\sim$12.7% of the network) as outliers with significant discrepancies; excluding these sites, the final evaluation considered 69 stations for the inter-solution comparison.

The horizontal velocity agreement among all PPP-AR solutions and the reference was very strong. Mean inter-solution horizontal differences were on the order of 0.05–0.6 mm yr^{-1}, with RMS differences below 1 mm yr^{-1} and Pearson correlation coefficients $R \geq 0.94$. Such small discrepancies are comparable to the formal uncertainties of global reference-frame velocities, indicating that, for this daily-static regional dataset, PPP-AR solutions provide horizontal velocity estimates strongly consistent with the network-constrained solution [14]. In practical terms, the horizontal velocity estimates from all processing strategies were mutually consistent at the sub-millimetre-per-year level.

By contrast, the vertical component showed larger differences and processing-strategy-dependent behaviour. Using the DD-minus-PPP convention of Table 5, Bernese PPP-AR shows a mean Up difference of $+1.05$ mm yr^{-1}, indicating lower Bernese PPP-AR vertical rates relative to the DD reference on average. PRIDE-PPP shows weaker vertical correlation ($R \approx 0.59$) and higher scatter (vertical RMS $\sim$1.32 mm yr^{-1}), while NGL/GipsyX has the highest vertical correlation ($R \approx 0.86$), the smallest vertical RMS ($\sim$0.7 mm yr^{-1}), and a small DD-minus-PPP mean difference ($+0.19$ mm yr^{-1}). These findings underscore that vertical velocities remain more challenging to estimate consistently, with results varying by processing strategy.

Overall, vertical velocity uncertainties were roughly two to three times larger than horizontal uncertainties, consistent with prior GNSS analyses [2,4]. The observed vertical differences likely reflect the cumulative influence of reference-frame realization, tropospheric modeling, loading and tidal corrections, observation weighting, precise products, ambiguity-resolution implementation, and stochastic constraints. Future controlled experiments under progressively unified processing configurations would be valuable for decomposing these effects, including the role of observation-system configuration and ambiguity-resolution strategy. Within the scope of the present daily-static comparison, the results support the practical use of operational PPP-AR products for long-term horizontal regional geodynamics, while highlighting the need for caution in vertical-rate interpretation.

Author Contributions: Conceptualization, S.M., A.Z., M.N., D.F., A.C. and L.V.; methodology, S.M., A.Z. and M.N.; software, S.M., A.Z., M.N., M.C. and G.D.C.; formal analysis, S.M.; data curation, S.M.; writing—original draft preparation, S.M.; writing—review and editing, A.Z., M.N., L.V. and S.M.; supervision, A.Z., M.N. and L.V. All authors have read and agreed to the published version of the manuscript.

Funding: This research was partially funded by the project PRIN2022 nr. 2022JLJ54N-01 (P.I. Filippo Greco).

Data Availability Statement: Publicly available datasets were analyzed in this study. GNSS observations and metadata were accessed through the EPOS GNSS Data Gateway. Additional GNSS time series were obtained from the Nevada Geodetic Laboratory (NGL). Precise orbit, clock, and bias products were provided by the Center for Orbit Determination in Europe (CODE). Processed time series, HectorP control settings, and analysis outputs are available from the corresponding author upon reasonable request.

Acknowledgments: The authors gratefully acknowledge the Istituto Nazionale di Geofisica e Vulcanologia (INGV) for providing access to the Rete Integrata Nazionale GPS (RING) data, as well as the International GNSS Service (IGS) and the EUREF Permanent Network (EPN) for the availability of high-quality GNSS observations and products. We thank the Center for Orbit Determination in Europe (CODE) for providing precise orbit, clock, and bias products used in this study, and the Nevada Geodetic Laboratory (NGL) for making their GNSS time series and products publicly available. GNSS data access and management were facilitated through the EPOS GNSS Data Gateway. D.F. acknowledges support from the European Union–NextGenerationEU through a PhD fellowship funded under the Italian National Recovery and Resilience Plan (PNRR) CUP H74D24001410004.

Conflicts of Interest: The authors declare no conflicts of interest.

References

1. Kenyeres, A.; Grau Bellet, J.; Bruyninx, C.; Caporali, A.; de Doncker, F.; Droscak, B.; Duret, A.; Franke, P.; Georgiev, I.; Bingley, R.; et al. Regional integration of long-term national dense GNSS network solutions. *GPS Solut.* **2019**, *23*, 122. [CrossRef]
2. Bitharis, S.; Pikridas, C.; Fotiou, A.; Rossikopoulos, D. GPS data analysis and geodetic velocity field investigation in Greece, 2001–2016. *GPS Solut.* **2024**, *28*, 16. [CrossRef]
3. Altamimi, Z.; Rebischung, P.; Collilieux, X.; Métivier, L.; Chanard, K. ITRF2020: An augmented reference frame refining the modeling of nonlinear station motions. *J. Geod.* **2023**, *97*, 47. [CrossRef]
4. Nistor, S.; Suba, N.-S.; Maciuk, K.; Kudrys, J.; Nastase, E.; Muntean, A. Analysis of Noise and Velocity in GNSS EPN-Repro 2 Time Series. *Remote Sens.* **2021**, *13*, 2783. [CrossRef]
5. He, X.; Montillet, J.-P.; Fernandes, R.; Bos, M.; Yu, K.; Hua, X.; Jiang, W. Review of current GPS methodologies for producing accurate time series and their error sources. *J. Geodyn.* **2017**, *106*, 12–29. [CrossRef]
6. Dach, R.; Andritsch, F.; Arnold, D.; Bertone, S.; Fridez, P.; Jäggi, A.; Jean, Y.; Maier, A.; Mervart, L.; Meyer, U.; et al. *Bernese GNSS Software Version 5.2*; Astronomical Institute, University of Bern: Bern, Switzerland, 2015. [CrossRef]
7. Herring, T.A.; King, R.W.; McClusky, S.C. *Introduction to GAMIT/GLOBK, Release 10.35*; Massachusetts Institute of Technology: Cambridge, MA, USA, 2008.
8. Zumberge, J.F.; Heflin, M.B.; Jefferson, D.C.; Watkins, M.M.; Webb, F.H. Precise point positioning for the efficient and robust analysis of GPS data from large networks. *J. Geophys. Res. Solid Earth* **1997**, *102*, 5005–5017. [CrossRef]
9. Kouba, J.; Héroux, P. Precise Point Positioning Using IGS Orbit and Clock Products. *GPS Solut.* **2001**, *5*, 12–28. [CrossRef]
10. Geng, J.; Chen, X.; Pan, Y.; Mao, S.; Li, C.; Zhou, J.; Zhang, K. PRIDE PPP-AR: An open-source software for GPS PPP ambiguity resolution. *GPS Solut.* **2019**, *23*, 91. [CrossRef]
11. Ogutcu, S.; Alcay, S.; Duman, H.; Özdemir, B.N.; Konukseven, C. Static and kinematic PPP-AR performance of low-cost GNSS receiver in monitoring displacements. *Adv. Space Res.* **2023**, *72*, 4795–4808. [CrossRef]
12. Chen, G.; Wei, N.; Tao, J.; Zhao, Q. Comparison between GPS network analysis with undifferenced and double differenced integer ambiguity resolution: A practical perspective. *Adv. Space Res.* **2024**, *74*, 582–595. [CrossRef]
13. García-Armenteros, J.A. Topo-Iberia CGPS network: A new 3D crustal velocity field in the Iberian Peninsula and Morocco based on 11 years (2008–2019). *GPS Solut.* **2023**, *27*, 155. [CrossRef]
14. Wang, R.; Chen, J.; Zhang, Y.; Tan, W.; Liao, X. Contribution of PPP with Ambiguity Resolution to the Maintenance of Terrestrial Reference Frame. *Remote Sens.* **2025**, *17*, 1183. [CrossRef]
15. Li, X.; Huang, J.; Li, X.; Shen, Z.; Han, J.; Li, L.; Wang, B. Review of PPP–RTK: Achievements, challenges, and opportunities. *Satell. Navig.* **2022**, *3*, 28. [CrossRef]
16. Williams, S.; Bock, Y.; Fang, P.; Jamason, P.; Nikolaidis, R.; Prawirodirdjo, L.; Miller, M.; Johnson, D. Error analysis of continuous GPS time series. *J. Geophys. Res. Solid Earth* **2004**, *109*, B03412. [CrossRef]
17. Vázquez-Ontiveros, J.R.; Padilla-Velazco, J.; Gaxiola-Camacho, J.R.; Vázquez-Becerra, G.E. Evaluation and Analysis of the Accuracy of Open-Source Software and Online Services for PPP Processing in Static Mode. *Remote Sens.* **2023**, *15*, 2034. [CrossRef]
18. Bos, M.; Fernandes, R.; Williams, S.; Bastos, M. Fast error analysis of continuous GNSS observations with missing data. *J. Geod.* **2013**, *87*, 351–360. [CrossRef]
19. EPOS. Data & Services: GNSS Data and Products. Available online: https://www.epos-eu.org/tcs/gnss-data-and-products/data-services (accessed on 1 January 2026).
20. Avallone, A.; Selvaggi, G.; D'Anastasio, E.; D'Agostino, N.; Pietrantonio, G.; Riguzzi, F.; Serpelloni, E.; Anzidei, M.; Casula, G.; Cecere, G.; et al. The RING network: Improvement of a GPS velocity field in the central Mediterranean. *Ann. Geophys.* **2010**, *53*, 39–54. [CrossRef]
21. EPOS. Data Providers and Agencies. Available online: https://gnss-epos.eu/dataproviders-agencies/ (accessed on 1 January 2026).
22. AVISO+; CNES. *FES2022 (Finite Element Solution) Ocean Tide*, Version 2024 [Data Set]; AVISO+: Ramonville St-Agne, France, 2024. [CrossRef]
23. Ray, R.D.; Ponte, R.M. Barometric tides from ECMWF operational analyses. *Ann. Geophys.* **2003**, *21*, 1897–1910. [CrossRef]
24. Petit, G.; Luzum, B. *IERS Conventions (2010)*; IERS Technical Note 36; Verlag des Bundesamts für Kartographie und Geodäsie: Frankfurt am Main, Germany, 2010.
25. Landskron, D.; Böhm, J. VMF3/GPT3: Refined discrete and empirical troposphere mapping functions. *J. Geod.* **2018**, *92*, 349–360. [CrossRef] [PubMed]
26. Chen, G.; Herring, T.A. Effects of atmospheric azimuthal asymmetry on the analysis of space geodetic data. *J. Geophys. Res. Solid Earth* **1997**, *102*, 20489–20502. [CrossRef]

27. Blewitt, G.; Hammond, W.; Kreemer, C. Harnessing the GPS Data Explosion for Interdisciplinary Science. *Eos* **2018**, *99*, 485. [CrossRef]
28. Nevada Geodetic Laboratory. Nevada Geodetic Laboratory Data Portal. Available online: https://geodesy.unr.edu/ (accessed on 1 January 2026).
29. Bland, J.M.; Altman, D.G. Statistical methods for assessing agreement between two methods of clinical measurement. *Lancet* **1986**, *327*, 307–310. [CrossRef]
30. Bland, J.M.; Altman, D.G. Measuring agreement in method comparison studies. *Stat. Methods Med. Res.* **1999**, *8*, 135–160. [CrossRef] [PubMed]

Disclaimer/Publisher's Note: The statements, opinions and data contained in all publications are solely those of the individual author(s) and contributor(s) and not of MDPI and/or the editor(s). MDPI and/or the editor(s) disclaim responsibility for any injury to people or property resulting from any ideas, methods, instructions or products referred to in the content.